

Machine-Learning enabled analysis of ELM filament  
dynamics in KSTAR

Cooper Jacobus,<sup>\*,a</sup> Minjun J. Choi,<sup>b</sup> and Ralph Kube<sup>c</sup>

<sup>a</sup>*University of California, Berkeley, CA 94720, USA*

<sup>b</sup>*Korea Institute of Fusion Energy, Daejeon 34133, Republic of Korea*

<sup>c</sup>*Princeton Plasma Physics Laboratory, NJ 08540, USA*

\*Email: [cjacobus@berkeley.edu](mailto:cjacobus@berkeley.edu)

Number of pages: 25

Number of tables: 0

Number of figures: 13

## Abstract

The emergence and dynamics of filamentary structures associated with edge-localized modes (ELMs) inside tokamak plasmas during high-confinement mode is regularly studied using Electron Cyclotron Emission Imaging (ECEI) diagnostic systems. Such diagnostics allow us to infer electron temperature variations, often across a poloidal cross-section. Previously, detailed analysis of these filamentary dynamics and classification of the precursors to edge-localized crashes has been done manually. We present a machine-learning-based model, capable of automatically identifying the position, spatial extend, and amplitude of ELM filaments. The model is a deep convolutional neural network that has been trained and optimized on an extensive set of manually labeled ECEI data from the KSTAR tokamak. Once trained, the model achieves a 93.7% precision and allows us to robustly identify plasma filaments in unseen ECEI data. The trained model is used to characterize ELM filament dynamics in a single H-mode plasma discharge. We identify quasi-periodic oscillations of the filaments size, total heat content, and radial velocity. The detailed dynamics of these quantities appear strongly correlated with each other and appear qualitatively different during the pre-crash and ELM crash phases.

**Keywords** — Machine Learning, Convolutional Neural Networks, Edge Localized Mode, Electron Cyclotron Emission Imaging

## I. INTRODUCTION

High confinement mode (H-mode) plasmas are characterized by a steep density gradient in the edge, the so-called pedestal region, of the confined plasma. Access to H-mode is achieved by plasma heating and once a critical heating threshold is exceeded the pedestal typically forms within a few milliseconds. Associated with this rapid transition are strong sheared electric drifts localized to the pedestal region as well as a local suppression of local turbulent fluctuations [1, 2, 3]. These sheared electric drifts form a transport barrier which inhibits radial transport. As a result, the energy confinement properties of H-mode plasmas are superior to those in low-confinement mode and render this mode of operation an attractive baseline scenario for ITER [4, 5]. Edge localized modes (ELMs) are a ubiquitous feature of H-mode plasmas. They cause an intermittent relaxation of the edge pressure gradient, caused by so-called ELM crashes. During these violent events, plasma ejects from the confined region onto material surfaces of the vacuum vessel. Upon contact with the hot plasma, material surfaces erode and sputtered wall atoms contaminate the confined plasma. These phenomena are at the core of complex research activities in the fusion community. Regulating impurities in magnetically confined plasmas, which includes both heavy wall impurities and fusion ash for future burning plasmas, is critical for their stable confinement [6]. Furthermore dictate transient heat loads from ELM cycles the desired properties of plasma facing components for magnetic fusion devices [7].

There are various types of ELM, identified based on periodicity and dependence on heating power. These types include violent, low-frequency Type-I ELMs, or more intermittent, burst-like Type-III ELMs, as well as a mixed regime [8, 9, 10]. While two-fold stability analysis of peeling-ballooning modes explains linear stability of ELMs [11, 12], the actual ELM crash is a nonlinear magnetohydrodynamic phenomenon and an area of active research interest [13, 3, 14, 15, 12].

At the KSTAR Tokamak, a two-dimensional (2D) Electron Cyclotron Emission imaging diagnostic [16, 17] has been used to investigate the nonlinear dynamics of ELMs, including their explosive growth, saturation, and crash [18, 19]. In the 2D ECE images, the ELM mode appears as a filamentary structure of the normalized temperature fluctuation near the pedestal top. The evolution of these ELM filaments is divided into three phases. During an initial growth phase, the amplitude of the mode structure increases while the structure itself rotates counterclockwise through the ECEI field of view. Once saturated, the ELM filament amplitude appears to stagnate

while the filaments continue their poloidal rotation. Finally, the ELM crash manifests itself as the circular shape transforms into finger-like structures that extend from the pedestal into the open field-line region. A similar phenomenology is reported from other tokamaks [20, 21, 22]. In order to investigate physical mechanisms that drive ELM filament dynamics and lead up to ELM crashes it is desirable to robustly estimate properties of the structures visible in the ECEI data. This includes for example the number of visible filaments, their amplitude, their spatial extent, and their velocities. With this information at hand, one can investigate all three phases, initial growth, saturation, as well as the ELM crash itself.

Besides ELM filaments, plasma filaments in scrape-off layer plasmas, often called blobs, present a similar foot-print in gas-puff imaging measurements [23]. Automatic detection of these structures has been performed using blob detection, which identifies coherent structures of a minimum size that exceed a heuristically determined amplitude threshold [24, 25, 26]. Other work approaches blob detection using cross-correlation based methods [27]. Only recently have machine learning methods been used to identify the extent of filament structures in fusion plasmas [28]. Machine-learning based models learn detection criteria based on labeled training data. That is, they don't require a-priori heuristically tuned parameters for structure detection but replace them with information encoded in expert-labeled training data. The approach presented here is of the same spirit and to the best knowledge of the authors a first attempt to use a machine-learning-based algorithm to investigate ELM filament dynamics.

The remainder of the article is structured as follows. In section II we introduce the used deep convolutional neural network architecture and describe its application for ECEI data. We also describe the developed training data set and the performance of the trained network on training and validation data sets. In section III we use the trained model to identify filamentary structures in a H-Mode plasma discharge and explore their dynamical properties. We discuss the results and set them into context with other recent work in IV. A conclusion and directions for future work are given in V

## II. MACHINE LEARNING DETECTION OF ELM FILAMENTS IN ECEI DATA

Cyclotron radiation emission from free electrons in magnetically confined plasmas are routinely measured for diagnostic purposes [16, 29]. At KSTAR, 2D ECEI systems are used to

measure electron temperature fluctuations  $\delta T_e / \langle T_e \rangle$  over a two-dimensional field of view aligned in the poloidal cross-section on a microsecond timescale. [16, 17]. Each system covers rectangular cross-sections of the plasma with 24 by 8 pixels in the vertical and radial direction respectively, featuring a spatial resolution of  $\lesssim 2\text{cm}$  and a sampling time of  $\lesssim 2\mu\text{s}$ . In practice, the low-field side field-of-view extends about 40 cm vertically and about 10 cm radially which readily allows us to visualize filamentary structures associated with ELMs.

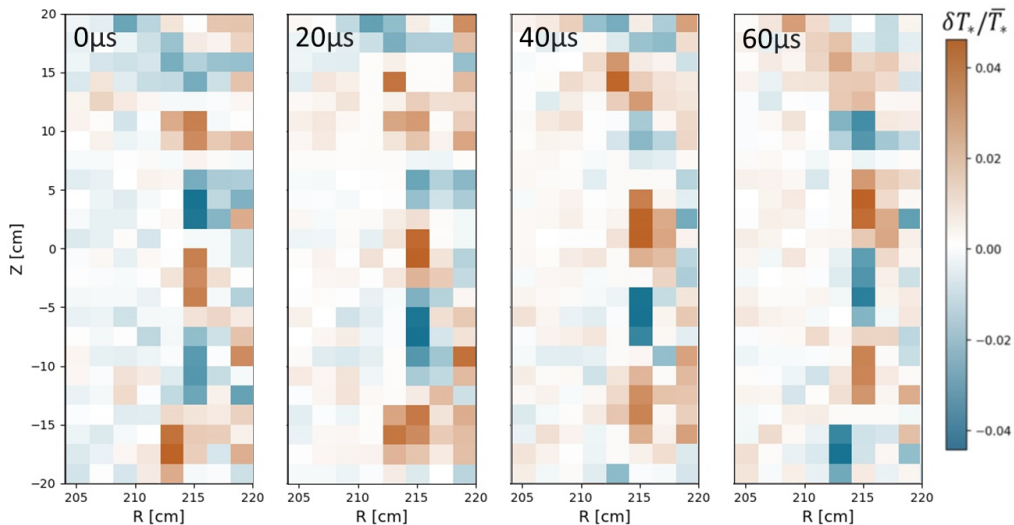


Fig. 1. A sequence of ECE images taken during the initial growth phase of an ELM. Humans readily identify a modal structure with peaks and troughs which rotates counter-clockwise in this image sequence.

Normalizing to vanishing mean, the emission intensity sampled by the ECE diagnostic can be interpreted as a temperature fluctuation  $\delta T / \langle T \rangle$ . The temperature corresponds to the radiation temperature and it is usually justified to associate it with the electron temperature [29, 16]. All ECE data used in this contribution is normalized this way, while pixels with low signal-to-noise ratio are replaced by a linear interpolant. The data was furthermore subject to a bandpass filter. Figure 1 shows a sequence of ECEI images that capture a mode structure associated with an ELM. To estimate the dynamics present in this sequence of images we can visually identify individual peaks and troughs in each image. Asserting that peaks (or troughs) in subsequent images with maximal overlap correspond to the same part of the observed mode structure, we estimate a rotation velocity of approximately 2 cm per  $20\mu\text{s}$  frame, that is, the modal structure rotates at

roughly 1km/s. A computer vision algorithm can automatically perform this calculation. For this, we need a detector that identifies individual peaks and an algorithm that can identify and track a given structure in a sequence of images.

In this contribution, we use a Scaled-YOLOv4 Scaled-YOLOv4 (You only look once) model [30, 31, 32] to identify such ELM filaments in ECEI data. YOLO is a widely used class of object detection models and the Scaled-YOLOv4 model modifies with original YOLO architecture in order to be applicable to smaller images. Object detection models, such as YOLO, are able to identify objects in image data by outputting bounding box pixels together with a class label for identified object instances. The YOLO model implements a convolutional neural network (CNN) architecture, where a sequence of learned filters, each followed by non-linear activation functions, is to the input data. The size and the stride as well as the number of output channels are fixed while the convolution matrix coefficients are trainable parameters. Besides its convolutional architecture, design choices in the YOLO architecture are made in order to optimize inference speed, which makes it one of the fastest image detection algorithms available [31]. YOLO models like this one have also been found to detect  $\sim 3$  times fewer false positives than other similar architectures [33].

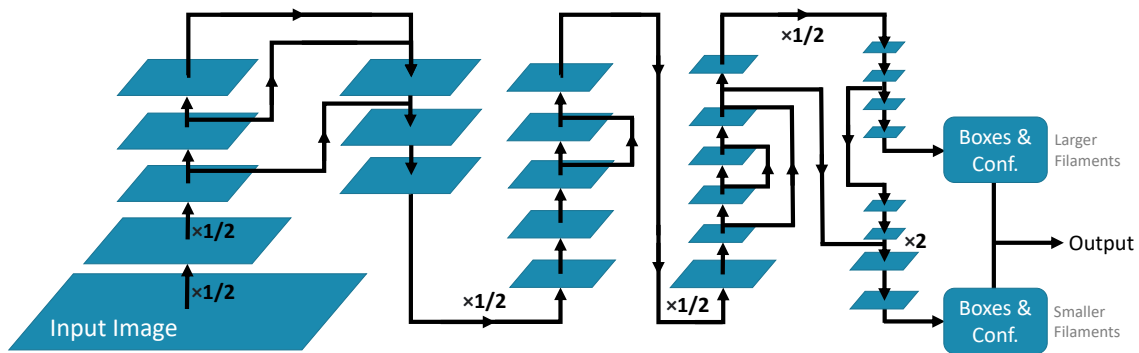


Fig. 2. Illustration of the convolutional architecture implemented by the used YOLOv4 model. Blue rectangles denote data at a given layer and their size is proportional to the matrix dimensions. Black arrows denote connections between layers, and are annotated by scale factors in the case where a convolution changes the layer size. There are two outputs layers, each of the giving a set of bounding boxes as well as a confidence score for detected instances of object classes in the input image.

Figure 2 illustrates the architecture of the used Scaled YOLOv4 network. The input is a 192-by-64 pixel image with 3 channels. To transform the normalized  $24 \times 8$  ECEI data frames to this size they are up-sampled using cubic interpolation and then a colormap is applied. The first

convolution applies a set of  $3 \times 3$  sized filter matrices with a stride of 2 and outputs  $32 \times 32 \times 32$  matrices, reducing the input resolution by a factor of 2. The resulting matrix is then used as input to the next layer. While connections are mostly between successive layers, YOLO also uses a number of residual connections, where the outputs of non-consecutive layers are concatenated along the channel dimension. The outputs of the YOLO network are two sets of bounding boxes with associated confidence scores. The first set of outputs is used to identify larger structures. Then, continuing processing through some more up-convolution layers, another output is generated that allows us to identify smaller structures. Reference [31] lists the details of the architecture. For work presented in this contribution, we used the scaled YOLO-v4 implementation provided here [a](#).

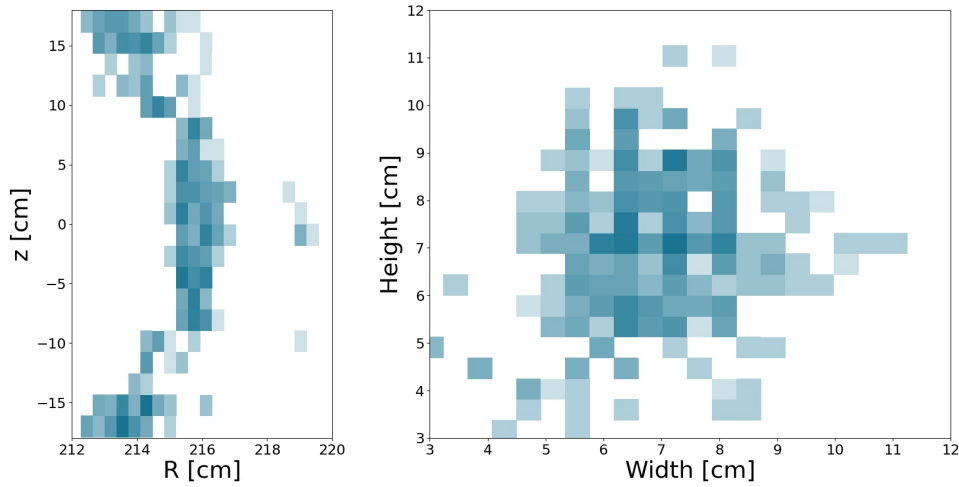


Fig. 3. Histograms of the anchor and linear sizes of the bounding boxes prescribed in the manually labelled training data.

YOLO is trained in a supervised fashion and requires labeled training data. We manually created a training set of ELM filaments by randomly selecting 1000 ECEI data frames and fitting tight bounding boxes around ELM filaments that appear in these frames. A bounding box is described by four values: an anchor point in the 2d ECEI view, a width, and a height. We only label hot filaments which contain excess heat and therefore all bounding boxes are assigned the same class. Figure 3 shows the distribution of bounding boxes in the training set. The

<sup>a</sup><https://github.com/AlexeyAB/darknet>

anchors appear mostly on a singular flux surfaces with some detections also at  $R \approx 220\text{cm}$  and  $Z \approx 0\text{cm}$ . The width and height of the bounding boxes distribution in the manually labeled data are approximately  $7 \pm 3\text{cm}$ . There are only a few outliers in the bounding box size distributions, either centered at smaller sizes or tall filaments with a width of approximately 10 cm and a height of approximately 7cm.

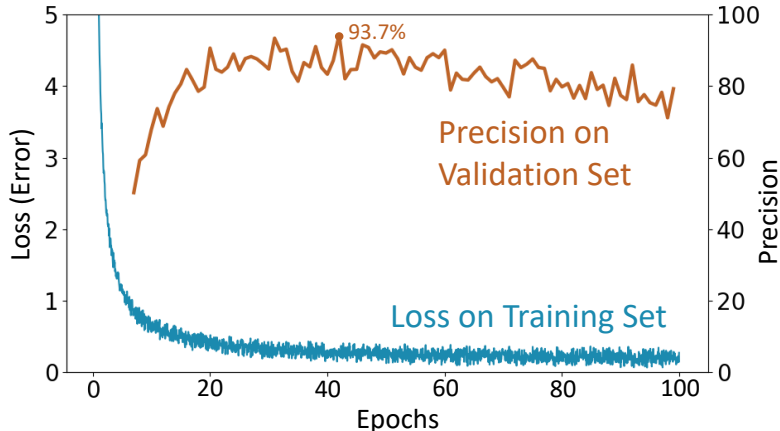


Fig. 4. Calculated values of YOLO loss on the training set and precision on the validation set during training.

The task of the trained model is to output tightly fitting bounding boxes with correct class labels around ELM filament instances in unseen data. YOLO uses a special loss function which is given by a weighted sum of multiple terms. These include a binary cross-entropy term for correct instance labeling as well as a term describing intersection-over-union (IoU) misalignment of the bounding boxes. Intersection over union is a commonly used quantity in object classification [31]. Given two boxes, IoU is calculated as the ratio over the intersection of the boxes to the union. For training, we randomly split the manually labeled data into a training set and a validation set, consisting respectively of 800 and 200 frames with their associated bounding boxes. The model parameters are optimized by minimizing the YOLO training loss function calculated over the training set for 100 epochs with a batch size of 64 randomly shuffled images and a learning rate of 0.00261.

Performance metrics of the model can readily be calculated from its IoU predictions. To aid in consuming the IoU information, it is common to identify a detection where  $IoU \geq 0.5$  as a true positive. Similarly, a false positive detection is an instance where  $IoU < 0.5$ . A false negative



detection is a case where the model identifies an object instance in an image where it is not present. And finally, a true negative detection is a case where the model does not identify object instances and they are not present in the image. During training, the performance of the model is monitored by tracking the value of the loss function calculated over the training set and the precision, the ratio between true positives to the sum of true and false positives, calculated on the validation set. The loss is minimized during training using the "Adam" optimizer. Figure 4 shows the training loss and validation precision of our model during training. Initially, the training loss decreases sharply and flattens after about 4000 iterations. At the same time, the precision on the validation set increases from about 60 to over 93% from iteration 1500 to 4000.

After training, the model achieves a 93.7% precision on the validation set. That is, it correctly captures the bounding box of the majority of labeled filaments. It also achieves a 85.2% recall, the ratio of true positives to the sum of true positives and false negatives. In other words, almost all detected filaments are indeed filaments present in the labeled data. On average, our model achieves 67.9% IoU, which highlights that there is still notable disagreement between the two. This stems however mostly from misalignment of the bounding boxes and not from misdetection of filaments.

Figure 5 illustrates how the trained YOLO model performs filament detection. The upper row shows the cubic interpolation of the ECEI data frames shown in 1 and the data frames shown in the lower row are taken from various phases of an observed ELM crash. The gray boxes denote manually labeled bounding boxes and predictions from the trained YOLO model are illustrated by black boxes. Visually inspecting the predictions we find that the center of the bounding boxes and their spatial extent corresponds well to the manual labels. During the saturated and the mid-crash phases, however, they appear to be more misaligned.

To investigate what degree of confidence is warranted in the predictions made by the trained YOLO model we plot histograms of the spatial distribution of the detection boxes on unseen data in figure 6 below. We find that the distribution of anchor points now extends radial out over a single flux surface. Since CNNs are equivariant under translation this alone warrants no loss of confidence in the predicted bounding boxes. But we furthermore observe that the distribution of bounding box dimensions exceeds those prescribed in the training data. Detected bounding boxes of smaller width and height, between 3 and 5 cm are frequently predicted but are absent in the training data. Since CNNs are not scale-invariant, these may be indicative of lower model

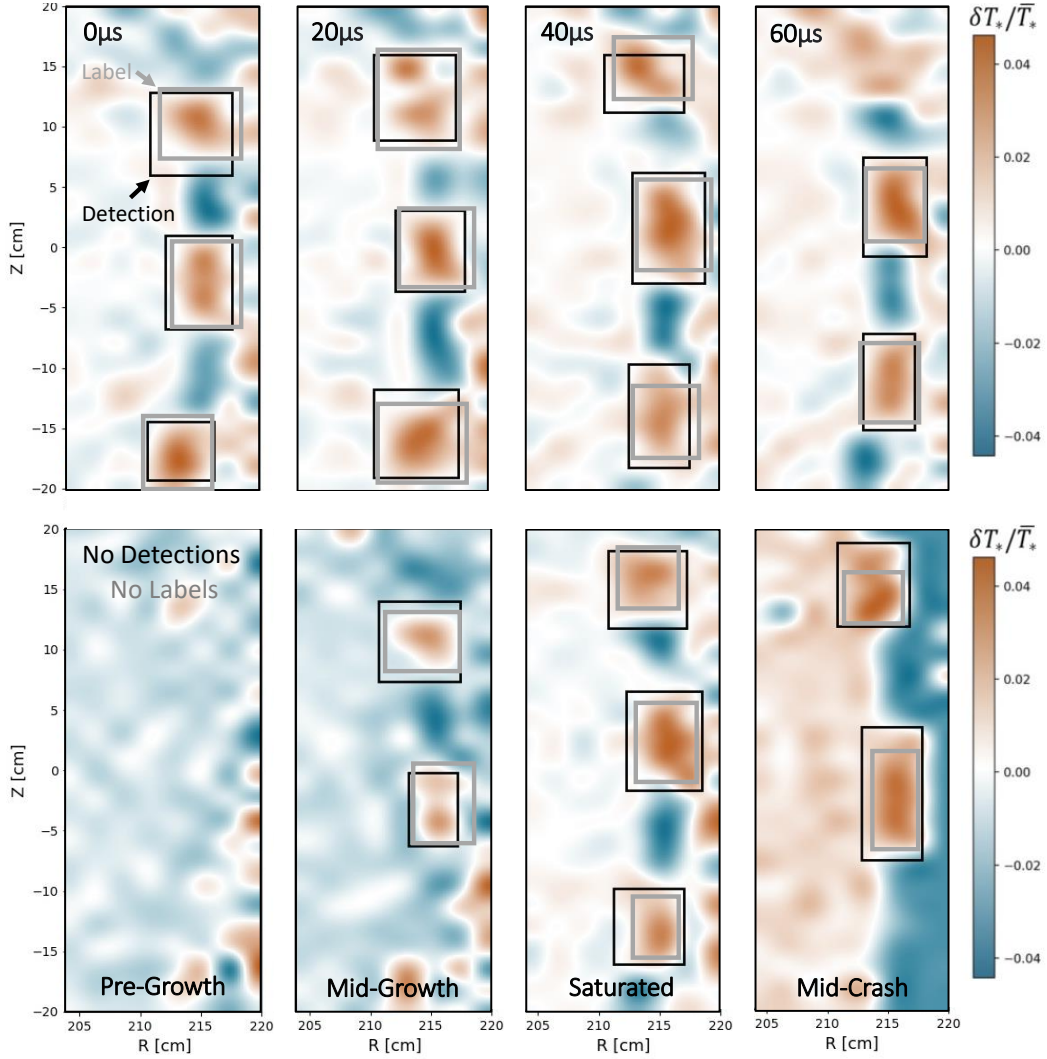


Fig. 5. Examples of ELM filament detection in ECEI images, performed by a trained YOLO model. The upper row corresponds to the images in figure 1 and the lower row corresponds to images during various stages in an ELM crash. The gray boxes denote manually labelled objects and the black boxes denote predictions from the YOLO model.

performance for tall and skinny or short and broad boxes. Examples of this can be seen in Fig.5 in the mid-growth and mid-crash frames, where tall and skinny predicted bounding boxes appear to feature lower IoU than predicted bounding boxes that appear more square-like.

Besides filament detection, the output of the trained YOLO model can be used to compile

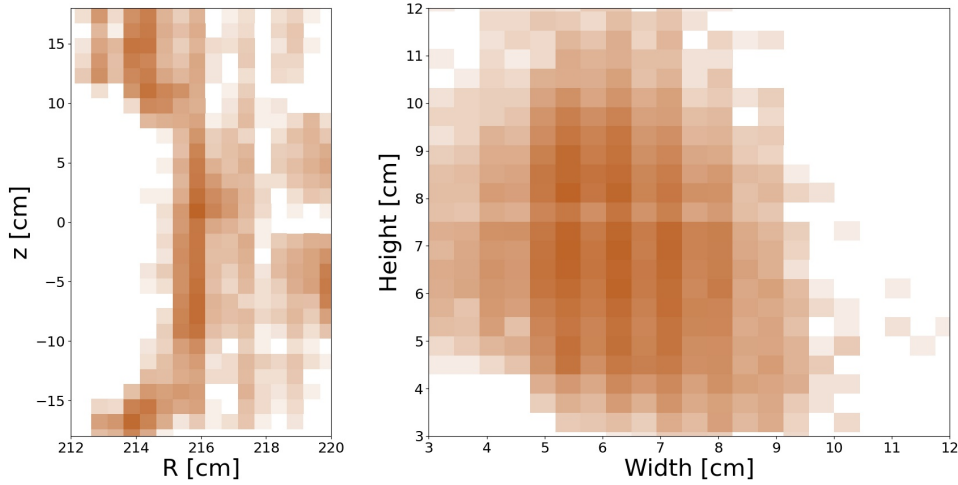


Fig. 6. Position and dimension distributions of the detection boxes for KSTAR shot 022289.

derived measurements, such as an average filament amplitude,  $\langle A \rangle$ .

$$\langle A \rangle = \frac{1}{N} \sum_{n=1}^N A_n \text{ where } A_n = \sum_{i,j \in \text{bbox } n} \left( \frac{\delta T}{\langle T \rangle} \right)_{i,j}^+. \quad (1)$$

This is just the average excess heat of all ELM filaments in a given ECEI frame. Here  $i$  and  $j$  index individual image pixels within a given bounding box and  $+$  indicates that this calculation considers only positive-valued pixels, ignoring the negative-valued pixels sometimes found in the corners of the bounding boxes.

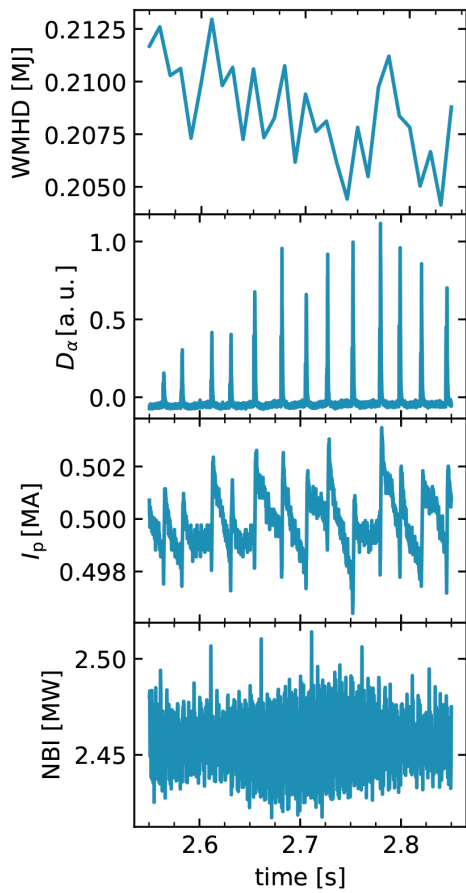
In order to track filament motion, bounding box centers are compared to connect detected filaments in subsequent frames with one another. Boxes in consecutive frames with centers within 2cm of each other are taken to be the same filament. Given a series of frames, filaments are first identified in all frames. Starting at the first frame, the identified filaments are connected with filaments from successor frames and their radial and poloidal velocity can be estimated using the center of the bounding box. If no successor filaments can be identified, no velocity is calculated. We also note here that the calculated filament velocities include contributions from background electric drifts. While these can readily be removed by calculating the radial electric field from a force balance model, here we focus only on properties of the filament tracking method developed. By detecting only peaks we do not assume any modal structure is present in the ECEI images.

This allows us to calculate filament amplitude statistics in all parts of the ELM crash development, from pre-growth to the final ELM crash.

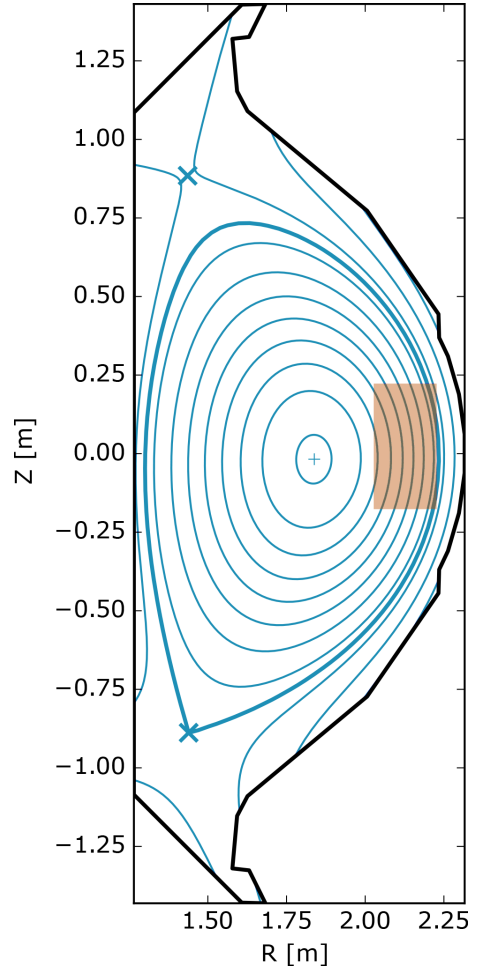
### III. DATA ANALYSIS

In the following, we use the trained YOLO model to investigate ELM filament dynamics for one H-mode plasma in KSTAR. This discharge features a toroidal magnetic field given by  $B_T = 1.8\text{T}$  and was neutral beam heated. Figure 7(a) shows time traces of the MHD energy, the emitted  $D_\alpha$  radiation, the plasma current, and the neutral beam power for shot 22289. The confined energy decreases and sharp peaks of the measured  $D_\alpha$  radiation indicate the presence of ELMs. The peaking frequency of  $D_\alpha$  and the plasma current  $I_p$  appear correlated while the neutral beam power remains approximately constant over the shown time slice. Figure 7(b) shows the magnetic equilibrium for this time slice, calculated using the EFIT [34] module in OMFIT [35]. The red rectangle denotes the field of view of the ECE diagnostic viewing the low-field side for which we report data analysis in the following. In addition to this discharge, we also investigate discharges 25086 and 25522, which show similar time traces and configuration of the ECEI field of view as shot 22289.

As a first step, we investigate how the average filament amplitude  $\langle A \rangle$ , defined in Eq.(1), behaves during ELM cycles. Figure 8 shows the time series of the spectrogram, calculated from ECEI data, together with the evolution of  $\langle A \rangle$ . Here, ELM crashes appear as short bursts of broadband fluctuation in the spectrogram. In the inter-ELM crash period, the ELM mode appears as a coherent fluctuation in the spectrogram and its frequency decreases with the pedestal recovery. Similarly,  $\langle A \rangle$  also peaks during the ELM crash. The time evolution of  $\langle A \rangle$ , which is carried by detected filaments, can visually be divided into three states. Immediately after an ELM crash,  $\langle A \rangle$  is approximately zero. The extent of this state appears to overlap with the frequency decreasing (pedestal recovery) period in the spectrogram in which the ELM amplitude may be too small to be detected clearly. After this phase,  $\langle A \rangle$  exhibits a larger mean and fluctuations. This phase extends approximately over the same time intervals where only slow frequencies below about 10 kHz appear in the spectrogram and precedes the ELM crash. During the actual ELM crash,  $\langle A \rangle$  sharply peaks to values up to 5 – 10, which is about two orders of magnitude larger than in the quiescent period that immediately follows the crash.



(a) Time traces of global plasma quantities for discharge 22289.



(b) Magnetic equilibrium reconstruction of shot 22289. The orange rectangle denotes the view of the ECEI diagnostic.

Fig. 7. Global plasma state and magnetic equilibrium reconstruction for shot 22289

We used our algorithm on multiple KSTAR shots other than 22289. It is worth noting that some other shots had no discernible modes or multiple modes which interact or a number of other significant differences.

Figure 9 shows time-traces of the average bounding box width and height for the detected filaments, calculated using a 0.01 s long moving average window. The shaded area denotes the standard deviation, calculated over the same interval as used for the moving average. Both, the average width and height undergo quasi-periodic oscillations that are correlated with the ELM crashes shown in 8. In the pre-crash phases, we observe average filament widths and heights of

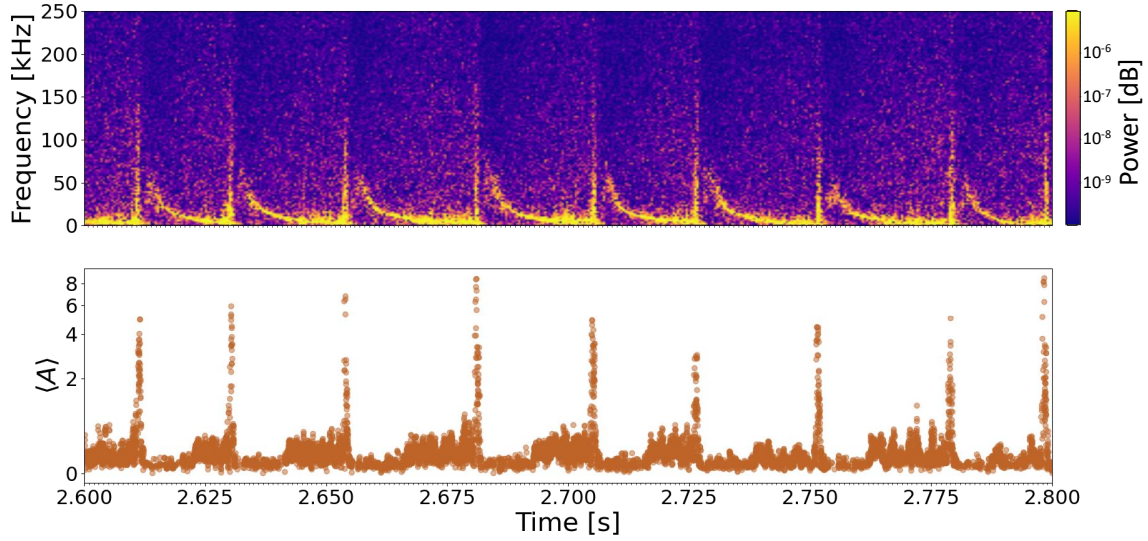


Fig. 8. Spectrogram and evolution of  $\langle A \rangle$  for shot 22289.

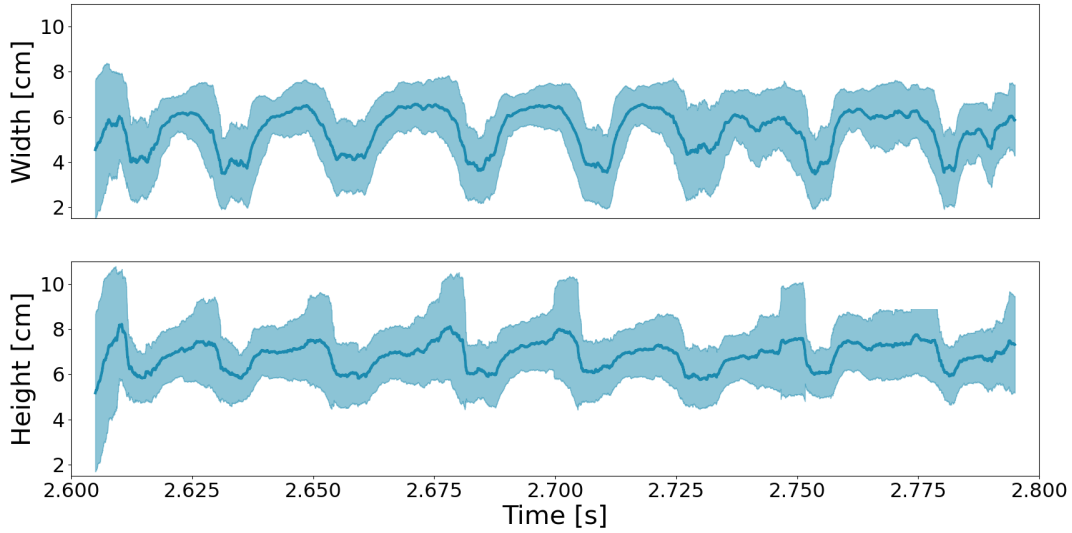


Fig. 9. Width and height of detected filaments in shot 22289

about 6 cm. In the period around the ELM crashes the detected width decreases to approximately 4 cm. The average height on the other hand shows only a minute average decrease but shows a much larger scatter in the period just before the ELM crash, indicating a significant change of the mode aspect ratio.

The average number of filaments detected in each frame, shown in Fig.10, shows similar quasi-periodic oscillations. Here the individual histograms are calculated over intervals of 5 ms. For the

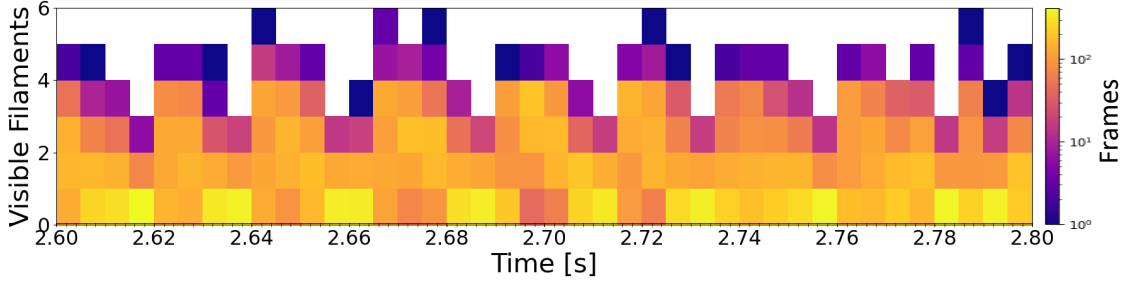


Fig. 10. Histogram of detected filament count in shot 22289.

pre-crash periods, the majority of frames feature zero to three filaments, but single frames show up to 5 detected filaments. During the ELM crash, the number of detected filaments decreases. Here, more frames are absent of any detected filaments and virtually no frames in this period have more than three detected frames.

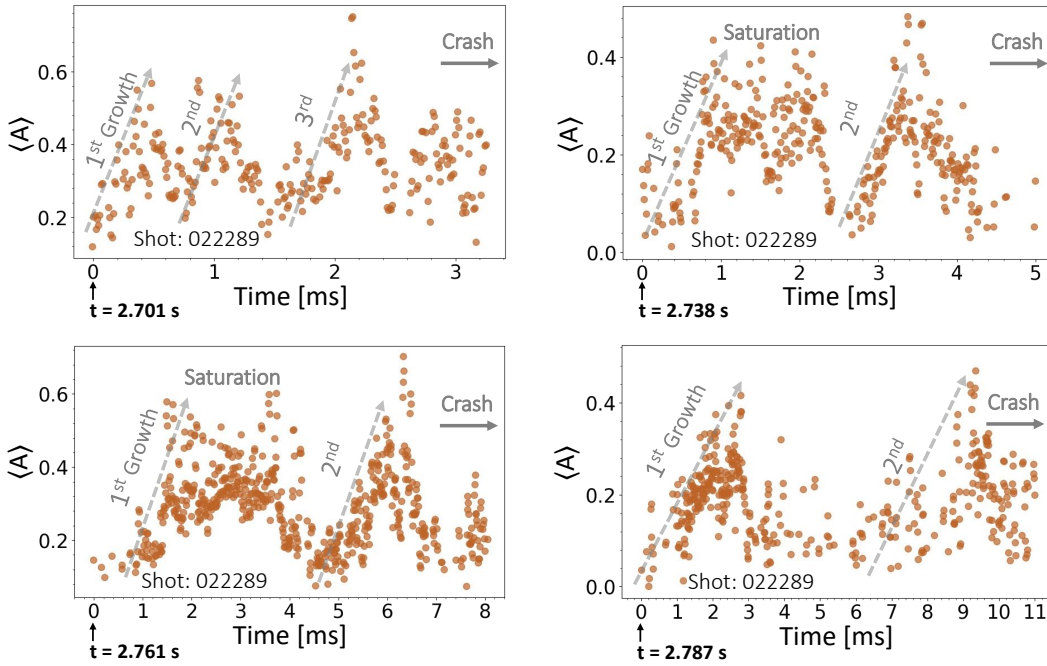


Fig. 11. Amplitude dynamics of ELM filaments in the interval leading up to ELM crash, as observed in shot 22289.

We continue by investigating the detailed filament dynamics during ELM crashes in shot 22289. Figure 11 shows the evolution of  $\langle A \rangle$  in a millisecond time interval right before ELM crashes. All four instances show short growth periods, where the total amount of heat contained

in the ELM filaments increases by a factor of 3 – 4. These growth periods may be followed by a saturation period where  $\langle A \rangle$  varies only little. But we also observe that after a short growth phase,  $\langle A \rangle$  returns to its initial value. Then  $\langle A \rangle$  may immediately begin to grow again, as observed for  $t = 2.701$  s or remain at a low value before growing again, as observed at  $t = 2.787$  s. The duration of the observed growth phases is about 1 ms, regardless of whether  $\langle A \rangle$  saturates afterwards or not.

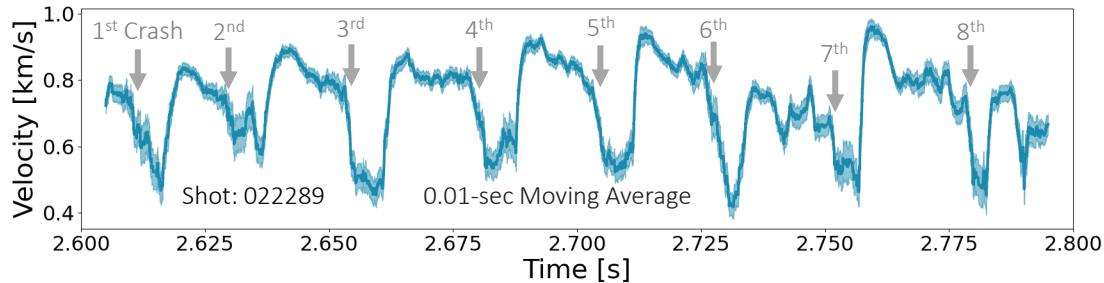


Fig. 12. Moving average of poloidal velocity observed in shot 22289.

We calculate the velocity of the ELM filaments by tracking them across frames. Figure 12 shows time series of the poloidal velocity and  $\langle A \rangle$  for shot 22289. The ELM crash period is correlated with a sharp drop in poloidal filament velocity. In the intervals leading up to an ELM, for example between  $t = 2.615 - 2.63$  s the poloidal velocity decreases slightly. While in other instances, for example during  $t = 2.66 - 2.68$  s, the poloidal velocity remains approximately constant. ELM crashes are associated with a rapid drop of the filament’s poloidal velocity. In some instances, for example at  $t = 2.615$  s the poloidal velocity immediately recovers to its pre-crash value while in other instances, for example at  $t = 2.655$  s, the poloidal velocity remains attenuated for a short interval.

Figure 13 visualizes the strong correlation cycle between filament amplitude and poloidal velocity observed in shot 22289. Tracked over 5 ELM crash cycles, we observe a hysteresis curve where first the poloidal velocity increases while  $\langle A \rangle$  remains constant. In the following pre-crash phase, the filament amplitude increases while the poloidal velocity remains constant. The ELM crash phase is then characterized by a drop in filament amplitude from approximately  $\langle A \rangle = 0.3$  to 0.1, and a simultaneous drop in filament velocity from approximately 1.0 km/s to 0.5 km/s.



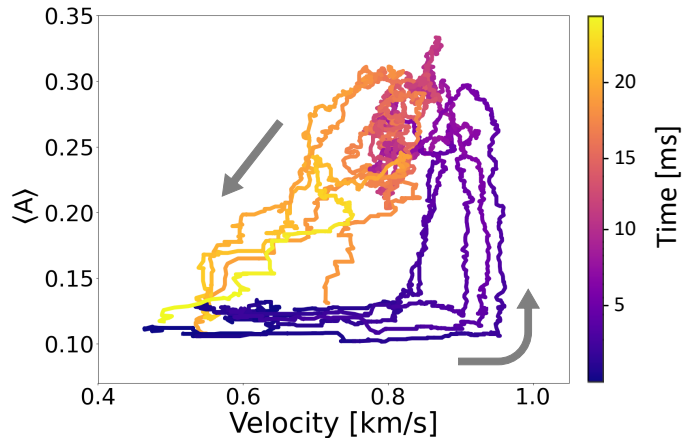


Fig. 13. Trajectory of the ELM crash in the space spanned by average filament amplitude  $\langle A \rangle$  and poloidal velocity. Time relative to an ELM crash is encoded in color. Five trajectories are overlaid.

#### IV. DISCUSSION

The Yolo-based detector reliably identifies ELM filaments in normalized ECEI images. As a supervised algorithm, the detector requires manually labeled training data to be able to detect ELM filaments in images. The trained detector achieves 93.7% accuracy on a validation set and manual inspection of predicted ELM filament bounding boxes shows a good performance across various stages of ELM development. Upon closer inspection, we find that the size distribution of the manually labeled data is more narrow than the distribution of bounding boxes recovered during inference. A manual inspection of the identified bounding boxes suggests that the mismatching part of the distribution is characterized by lower IoU scores. But regardless, the predicted bounding boxes still reliably identify ELM filaments. This effect highlights the sensitivity of supervised machine learning models to the biases included in the training data. In general, one needs to take care of imbalance issues when developing data-driven methods and carefully compare the properties of the training data set and the data set identified during inference.

The trained detector is used to identify individual ELM filament crests for a 0.2 s long sub-interval of an ELM cycle. From the detection events, we calculate the average width and height, filament amplitude, as well as poloidal velocity. The bounding box dimensions of the detected filaments, as well as the count of detected filaments present quasi-periodic behavior that is strongly correlated with the spectrogram as well as  $\langle A \rangle$ . Identifying the change of the bounding box as the mode-number of the ELM, this behavior is indicative of non-linear interactions which modify the

wavelength of the temperature perturbations. In particular, the width of the detected filaments changes from approximately 6 cm before ELM crashes to approximately 4 cm during the ELM crash. That is, by a factor of 1.5. At the same time, far fewer but hotter filaments are detected on average during the ELM crash.

A detailed analysis of  $\langle A \rangle$  in the periods leading up to an ELM crash shows a range of behaviors. Small growth phases can be followed by an intermediate saturation and reversals. This dithering between a ground state and a small elevated level appears random and no dynamics that are predictive of a following ELM crash are observed in the analyzed data.

Finally, we find a strong correlation between  $\langle A \rangle$  and the poloidal filament velocity. Each ELM crash is associated with a decrease in rotation velocity from about 0.8 km/s to about 0.4 km/s. After the ELM crash, the poloidal velocity rapidly recovers to pre-crash levels. In the data shown here, there appears no characteristic time scale for any decrease or increase in poloidal rotation velocity. For some ELM crashes, such as the first or the 6th ELM crash shown in 12. Finally, we show that the ELM cycle as observed in this single plasma follows a cyclical dynamic in the state space spanned by  $\langle A \rangle$  and the poloidal velocity.

By detecting individual ELM filaments on a frame-by-frame basis, the machine-learning-based detector allows us to infer the filament velocity also on a frame-by-frame basis. This is a major improvement over previous methods, where only average mode velocities are manually estimated from data, as described for example in [36]. The observed velocities of about 0.5 – 1.0 km/s are similar to poloidal velocities reported at ASDEX upgrade [37, 36]. We note here that the reported references are relative to the lab frame. Following an ELM crash, all measured revert to the values observed before the crash. and we don't observe random changes in mode number which have been reported for KSTAR plasmas [38].

## V. SUMMARY AND OUTLOOK

We use a machine learning model, based on the YOLO-v4 classifier, to detect ELM filaments in ECEI images. The developed detector performs robustly and is used to identify bounding boxes of ELM filaments during a 0.2 s long sub-interval. This data is used to investigate ELM filament dynamics. In particular, we compile linear sizes, the average ELM filament amplitude, as well as the poloidal velocity of the filaments in the laboratory frame. For the analyzed ELM crashes, all

these quantities present quasi-periodic behavior. Right after an ELM crash, the average filament amplitude is low, the average filament is about 8 cm wide and 8 cm tall and rotates counter-clockwise with about 0.8 km/s. Leading up to an ELM crash, the average filament amplitude increases, and their width, as well as poloidal velocity, decreases. The average number of filaments visible per frame also decreases in the period leading up to an ELM crash. In other words, ELM crashes manifest as few, hot filaments. The quasi-periodic behavior can be interpreted as closed cycles in the phase space spanned by  $\langle A \rangle$  and the poloidal velocity.

Future work will focus on systematic investigations of ECEI data sampled during ELM cycles. The possibility to automatically collect variations in filament properties on a frame-by-frame basis may for example more targeted investigations into non-linear evolution of the underlying peeling-ballooning mode physics. And finally, it may be desirable to condense the convolutional architecture of the used YOLO model into a simpler one, with still enough flexibility to identify ELM filaments in ECEI data. This may allow us to use less training data while keeping high detection accuracy.

## VI. ACKNOWLEDGEMENTS

This work was made possible by funding from the Department of Energy for the Summer Undergraduate Laboratory Internship (SULI) program. This work is supported by the US DOE Contract No. DE-AC02-09CH11466. The authors report no conflicts of interest.

## REFERENCES

- [1] R. A. MOYER, K. H. BURRELL, T. N. CARLSTROM, S. CODA, R. W. CONN, E. J. DOYLE, P. GOHIL, R. J. GROEBNER, J. KIM, R. LEHMER, W. A. PEEBLES, M. PORKOLAB, C. L. RETTIG, T. L. RHODES, R. P. SERAYDARIAN, R. STOCKDALE, D. M. THOMAS, G. R. TYNAN, and J. G. WATKINS, “Beyond paradigm: Turbulence, transport, and the origin of the radial electric field in low to high confinement mode transitions in the DIII-D tokamak,” *Physics of Plasmas*, **2**, 6, 2397 (1995); 10.1063/1.871263., URL <https://doi.org/10.1063/1.871263>.

- [2] F. WAGNER, “A quarter-century of H-mode studies,” *Nuclear Fusion*, **49**, 12B, B1 (2007); 10.1088/0741-3335/49/12b/s01., URL <https://doi.org/10.1088/0741-3335/49/12b/s01>.
- [3] A. W. LEONARD, “Edge-localized-modes in tokamaks,” *Physics of Plasmas*, **21**, 9, 090501 (2014); 10.1063/1.4894742., URL <https://doi.org/10.1063/1.4894742>.
- [4] I. A. E. AGENCY, *ITER Technical Basis*, no. 24 in ITER EDA Documentation Series, INTERNATIONAL ATOMIC ENERGY AGENCY, Vienna (2002)URL <https://www.iaea.org/publications/6492/iter-technical-basis>.
- [5] S. KIM, T. CASPER, and J. SNIPES, “Investigation of key parameters for the development of reliable ITER baseline operation scenarios using CORSICA,” *Nuclear Fusion*, **58**, 5, 056013 (2018); 10.1088/1741-4326/aab034., URL <https://doi.org/10.1088/1741-4326/aab034>.
- [6] C. ANGIONI, “Impurity transport in tokamak plasmas, theory, modelling and comparison with experiments,” *Plasma Physics and Controlled Fusion*, **63**, 7, 073001 (2021); 10.1088/1361-6587/abfc9a., URL <https://doi.org/10.1088/1361-6587/abfc9a>.
- [7] S. BREZINSEK, J. COENEN, T. SCHWARZ-SELINGER ET AL., “Plasma-wall interaction studies within the EUROfusion consortium: progress on plasma-facing components development and qualification,” *Nuclear Fusion*, **57**, 11, 116041 (2017); 10.1088/1741-4326/aa796e., URL <https://doi.org/10.1088/1741-4326/aa796e>.
- [8] D. HILL, “A review of ELMs in divertor tokamaks,” *Journal of Nuclear Materials*, **241-243**, 182 (1997); [https://doi.org/10.1016/S0022-3115\(97\)80039-6](https://doi.org/10.1016/S0022-3115(97)80039-6)., URL <https://www.sciencedirect.com/science/article/pii/S0022311597800396>.
- [9] G. LEE, M. KWON, C. DOH, B. HONG, K. KIM, M. CHO, W. NAMKUNG, C. CHANG, Y. KIM, J. KIM, H. JHANG, D. LEE, K. YOU, J. HAN, M. KYUM, J. CHOI, J. HONG, W. KIM, B. KIM, J. CHOI, S. SEO, H. NA, H. LEE, S. LEE, S. YOO, B. LEE, Y. JUNG, J. BAK, H. YANG, S. CHO, K. IM, N. HUR, I. YOO, J. SA, K. HONG, G. KIM, B. YOO, H. RI, Y. OH, Y. KIM, C. CHOI, D. KIM, Y. PARK, K. CHO, T. HA, S. HWANG, Y. KIM, S. BAANG, S. LEE, H. CHANG, W. CHOE, S. JEONG, S. OH, H. LEE, B. OH, B. CHOI, C. HWANG, S. IN, S. JEONG, I. KO, Y. BAE, H. KANG, J. KIM, H. AHN, D. KIM, C. CHOI, J. LEE, Y. LEE, Y. HWANG, S. HONG, K.-H. CHUNG, D.-I. CHOI, and K. TEAM, “Design

- and construction of the KSTAR tokamak,” *Nuclear Fusion*, **41**, 10, 1515 (2001); 10.1088/0029-5515/41/10/318., URL <https://doi.org/10.1088/0029-5515/41/10/318>.
- [10] J.-W. AHN, H.-S. KIM, Y. PARK, L. TERZOLO, W. KO, J.-K. PARK, A. ENGLAND, S. YOON, Y. JEON, S. SABBAGH, Y. BAE, J. BAK, S. HAHN, D. HILLIS, J. KIM, W. KIM, J. KWAK, K. LEE, Y. NA, Y. NAM, Y. OH, and S. PARK, “Confinement and ELM characteristics of H-mode plasmas in KSTAR,” *Nuclear Fusion*, **52**, 11, 114001 (2012); 10.1088/0029-5515/52/11/114001., URL <https://doi.org/10.1088/0029-5515/52/11/114001>.
- [11] P. B. SNYDER, H. R. WILSON, and X. Q. XU, “Progress in the peeling-ballooning model of edge localized modes: Numerical studies of nonlinear dynamics,” *Physics of Plasmas*, **12**, 5, 056115 (2005); 10.1063/1.1873792., URL <https://doi.org/10.1063/1.1873792>.
- [12] C. HAM, A. KIRK, S. PAMELA, and H. WILSON, “Filamentary plasma eruptions and their control on the route to fusion energy,” *Nature Reviews Physics*, **2**, 3, 159 (2020); 10.1038/s42254-019-0144-1., URL <https://doi.org/10.1038/s42254-019-0144-1>.
- [13] P. SNYDER, R. GROEBNER, J. HUGHES, T. OSBORNE, M. BEURSKENS, A. LEONARD, H. WILSON, and X. XU, “A first-principles predictive model of the pedestal height and width: development, testing and ITER optimization with the EPED model,” *Nuclear Fusion*, **51**, 10, 103016 (2011); 10.1088/0029-5515/51/10/103016., URL <https://doi.org/10.1088/0029-5515/51/10/103016>.
- [14] Y. OH, H. J. HWANG, M. LECONTE, M. KIM, and G. S. YUN, “Effect of time-varying flow-shear on the nonlinear stability of the boundary of magnetized toroidal plasmas,” *AIP Advances*, **8**, 2, 025224 (2018); 10.1063/1.5006554., URL <https://doi.org/10.1063/1.5006554>.
- [15] S. KIM, S. PAMELA, O. KWON, M. BECOULET, G. HUIJSMANS, Y. IN, M. HOELZL, J. LEE, M. KIM, G. PARK, H. S. KIM, Y. LEE, G. CHOI, C. LEE, A. KIRK, A. THORNTON, and Y.-S. N. AND, “Nonlinear modeling of the effect of  $n = 2$  resonant magnetic field perturbation on peeling-ballooning modes in KSTAR,” *Nuclear Fusion*, **60**, 2, 026009 (2020); 10.1088/1741-4326/ab5cf0., URL <https://doi.org/10.1088/1741-4326/ab5cf0>.

- [16] G. S. YUN, W. LEE, M. J. CHOI, J. B. KIM, H. K. PARK, C. W. DOMIER, B. TOBIAS, T. LIANG, X. KONG, N. C. LUHMANN, and A. J. H. DONNÉ, “Development of KSTAR ECE imaging system for measurement of temperature fluctuations and edge density fluctuations,” *Review of Scientific Instruments*, **81**, 10, 10D930 (2010); 10.1063/1.3483209., URL <https://doi.org/10.1063/1.3483209>.
- [17] G. S. YUN, W. LEE, M. J. CHOI, J. LEE, M. KIM, J. LEEM, Y. NAM, G. H. CHOE, H. K. PARK, H. PARK, D. S. WOO, K. W. KIM, C. W. DOMIER, N. C. LUHMANN, N. ITO, A. MASE, and S. G. LEE, “Quasi 3D ECE imaging system for study of MHD instabilities in KSTAR,” *Review of Scientific Instruments*, **85**, 11, 11D820 (2014); 10.1063/1.4890401., URL <https://doi.org/10.1063/1.4890401>.
- [18] G. S. YUN, W. LEE, M. J. CHOI, J. LEE, H. K. PARK, C. W. DOMIER, N. C. LUHMANN, B. TOBIAS, A. J. H. DONNÉ, J. H. LEE, Y. M. JEON, and S. W. YOON, “Two-dimensional imaging of edge-localized modes in KSTAR plasmas unperturbed and perturbed by n=1 external magnetic fields,” *Physics of Plasmas*, **19**, 5, 056114 (2012); 10.1063/1.3694842., URL <https://doi.org/10.1063/1.3694842>.
- [19] H. K. PARK, “Newly uncovered physics of MHD instabilities using 2-D electron cyclotron emission imaging system in toroidal plasmas,” *Advances in Physics: X*, **4**, 1, 1633956 (2019); 10.1080/23746149.2019.1633956., URL <https://doi.org/10.1080/23746149.2019.1633956>.
- [20] J. A. BOEDO, D. L. RUDAKOV, E. HOLLMANN, D. S. GRAY, K. H. BURRELL, R. A. MOYER, G. R. MCKEE, R. FONCK, P. C. STANGEBY, T. E. EVANS, P. B. SNYDER, A. W. LEONARD, M. A. MAHDAVI, M. J. SCHAFFER, W. P. WEST, M. E. FENSTERMACHER, M. GROTH, S. L. ALLEN, C. LASNIER, G. D. PORTER, N. S. WOLF, R. J. COLCHIN, L. ZENG, G. WANG, J. G. WATKINS, and T. TAKAHASHI, “Edge-localized mode dynamics and transport in the scrape-off layer of the DIII-D tokamak,” *Physics of Plasmas*, **12**, 7, 072516 (2005); 10.1063/1.1949224., URL <https://doi.org/10.1063/1.1949224>.
- [21] J. TERRY, I. CZIEGLER, A. HUBBARD, J. SNIPES, J. HUGHES, M. GREENWALD, B. LABOMBARD, Y. LIN, P. PHILLIPS, and S. WUKITCH, “The dynamics and structure of edge-localized-modes in Alcator C-Mod,” *Journal of Nuclear Materials*, **363-365**, 994

- (2007); <https://doi.org/10.1016/j.jnucmat.2007.01.266>., URL <https://www.sciencedirect.com/science/article/pii/S0022311507002048>, plasma-Surface Interactions-17.
- [22] R. J. MAQUEDA and R. MAINGI, “Primary edge localized mode filament structure in the National Spherical Torus Experiment,” *Physics of Plasmas*, **16**, 5, 056117 (2009); 10.1063/1.3085798., URL <https://doi.org/10.1063/1.3085798>.
- [23] S. J. ZWEBEN, D. P. STOTLER, J. L. TERRY, B. LABOMBARD, M. GREENWALD, M. MUTERSPAUGH, C. S. PITCHER, K. HALLATSCHKEK, R. J. MAQUEDA, B. ROGERS, J. L. LOWRANCE, V. J. MASTROCOLA, and G. F. RENDA, “Edge turbulence imaging in the Alcator C-Mod tokamak,” *Physics of Plasmas*, **9**, 5, 1981 (2002); 10.1063/1.1445179., URL <http://dx.doi.org/10.1063/1.1445179>.
- [24] R. KUBE, O. GARCIA, B. LABOMBARD, J. TERRY, and S. ZWEBEN, “Blob sizes and velocities in the Alcator C-Mod scrape-off layer,” *Journal of Nuclear Materials*, **438**, S505 (2013); <https://doi.org/10.1016/j.jnucmat.2013.01.104>., URL <https://www.sciencedirect.com/science/article/pii/S0022311513001128>, proceedings of the 20th International Conference on Plasma-Surface Interactions in Controlled Fusion Devices.
- [25] S. ZWEBEN, W. DAVIS, S. KAYE, J. MYRA, R. BELL, B. LEBLANC, R. MAQUEDA, T. MUNSAT, S. SABBAGH, Y. SECHREST, and D. S. AND, “Edge and SOL turbulence and blob variations over a large database in NSTX,” *Nuclear Fusion*, **55**, 9, 093035 (2015); 10.1088/0029-5515/55/9/093035., URL <https://doi.org/10.1088/0029-5515/55/9/093035>.
- [26] G. DECRISTOFORO, F. MILITELLO, T. NICHOLAS, J. OMOTANI, C. MARSDEN, N. WALKDEN, and O. E. GARCIA, “Blob interactions in 2D scrape-off layer simulations,” *Physics of Plasmas*, **27**, 12, 122301 (2020); 10.1063/5.0021314., URL <https://doi.org/10.1063/5.0021314>.
- [27] M. AGOSTINI, J. TERRY, P. SCARIN, and S. ZWEBEN, “Edge turbulence in different density regimes in Alcator C-Mod experiment,” *Nuclear Fusion*, **51**, 5, 053020 (2011); 10.1088/0029-5515/51/5/053020., URL <https://doi.org/10.1088/0029-5515/51/5/053020>.
- [28] M. IMRE, J. HAN, J. DOMINSKI, M. CHURCHILL, R. KUBE, C.-S. CHANG, T. PETERKA, H. GUO, and C. WANG, “ContourNet: Salient Local Contour Identification for Blob Detection in Plasma Fusion Simulation Data,” G. BEBIS, R. BOYLE, B. PARVIN, D. KORACIN,

- D. USHIZIMA, S. CHAI, S. SUEDA, X. LIN, A. LU, D. THALMANN, C. WANG, and P. XU (Editors), Advances in Visual Computing, 289–301, Springer International Publishing, Cham (2019).
- [29] I. H. HUTCHINSON, Principles of Plasma Diagnostics, Cambridge University Press (2002); 10.1017/CBO9780511613630.
- [30] J. REDMON, S. K. DIVVALA, R. B. GIRSHICK, and A. FARHADI, “You Only Look Once: Unified, Real-Time Object Detection,” CoRR, **abs/1506.02640** (2015)URL <http://arxiv.org/abs/1506.02640>.
- [31] A. BOCHKOVSKIY, C.-Y. WANG, and H.-Y. M. LIAO, “YOLOv4: Optimal Speed and Accuracy of Object Detection,” (2020).
- [32] C. WANG, A. BOCHKOVSKIY, and H. M. LIAO, “Scaled-YOLOv4: Scaling Cross Stage Partial Network,” CoRR, **abs/2011.08036** (2020)URL <https://arxiv.org/abs/2011.08036>.
- [33] L. JIAO, F. ZHANG, F. LIU, S. YANG, L. LI, Z. FENG, and R. QU, “A Survey of Deep Learning-based Object Detection,” CoRR, **abs/1907.09408** (2019)URL <http://arxiv.org/abs/1907.09408>.
- [34] L. LAO, H. S. JOHN, R. STAMBAUGH, and W. PFEIFFER, “Separation of beta-p and l-i in tokamaks of non-circular cross-section,” Nuclear Fusion, **25**, 10, 1421 (1985); 10.1088/0029-5515/25/10/004., URL <https://doi.org/10.1088/0029-5515/25/10/004>.
- [35] O. MENEGHINI, S. SMITH, L. LAO, O. IZACARD, Q. REN, J. PARK, J. CANDY, Z. WANG, C. LUNA, V. IZZO, B. GRIERSON, P. SNYDER, C. HOLLAND, J. PENNA, G. LU, P. RAUM, A. MCCUBBIN, D. ORLOV, E. BELLI, N. FERRARO, R. PRATER, T. OSBORNE, A. TURNBULL, and G. STAEBLER, “Integrated modeling applications for tokamak experiments with OMFIT,” Nuclear Fusion, **55**, 8, 083008 (2015)URL <http://iopscience.iop.org/article/10.1088/0029-5515/55/8/083008/meta>.
- [36] B. VANOVAC, E. WOLFRUM, M. HOELZL, M. WILLENSDORFER, M. CAVEDON, G. HARRER, F. MINK, S. DENK, S. FREETHY, M. DUNNE, P. MANZ, and N. L. AND, “Characterization of low-frequency inter-ELM modes of H-mode discharges at ASDEX Upgrade,” Nuclear



Fusion, **58**, 11, 112011 (2018); 10.1088/1741-4326/aada20., URL <https://doi.org/10.1088/1741-4326/aada20>.

[37] J. BOOM, I. CLASSEN, P. DE VRIES, T. EICH, E. WOLFRUM, W. SUTTROP, R. WENNINGER, A. DONNÉ, B. TOBIAS, C. DOMIER, N. LUHMANN, and H. P. AND, “2D ECE measurements of type-I edge localized modes at ASDEX Upgrade,” Nuclear Fusion, **51**, 10, 103039 (2011); 10.1088/0029-5515/51/10/103039., URL <https://doi.org/10.1088/0029-5515/51/10/103039>.

[38] J. LEE, G. YUN, M. KIM, J. LEE, W. LEE, H. PARK, C. DOMIER, N. LUHMANN, and W. K. AND, “Toroidal mode number transition of the edge localized modes in the KSTAR plasmas,” Nuclear Fusion, **55**, 11, 113035 (2015); 10.1088/0029-5515/55/11/113035., URL <https://doi.org/10.1088/0029-5515/55/11/113035>.